Characterization of the deformation and phase transformation behavior of VC-free and VC-containing FeMnSi-based shape memory alloys by *in situ* neutron diffraction

C. Leinenbach[1], A. Arabi-Hashemi[1], W.J. Lee[1,2], A. Lis[1,3], M. Sadegh-Ahmadi[1], S. Van Petegem[4], T. Panzner[5], H. Van Swygenhoven[4,6]

[1]Empa, Swiss Federal Laboratories for Materials Science and Technology, Überlandstrasse 129, CH-8600 Dübendorf, Switzerland

[2]Korea Institute of Industrial Technology, Jisa-dong, Gangseo-gu, Busan 618-230, Republic of Korea

[3]Division of Materials and Manufacturing Science, Graduate School of Engineering, Osaka University, Suita, Japan

[4]Swiss Light Source, Paul Scherrer Institut, CH-5232 Villigen PSI, Switzerland

[5]Laboratory for Neutron Scattering, NUM, Paul Scherrer Institut, CH-5232 Villigen PSI, Switzerland

[6]Neutrons and Xrays for Mechanics of Materials, IMX, Ecole Polytechnique Fédérale de Lausanne, CH-1012 Lausanne, Switzerland

Abstract:

The stress-induced fcc-austenite to hcp-martensite transformation in the iron based shape memory alloy (SMA) Fe-17Mn-5Si-10Cr-4Ni with and without VC precipitates is investigated by in-situ neutron diffraction measurements upon uniaxial loading and unloading. Based on experimentally derived elastic moduli the critical resolved shear stress (CRSS) for the fcc to hcp phase transformation was calculated. VC precipitates promote the martensite transformation by shifting the CRSS from 152 MPa to 85 MPa. A nearly perfect plastic behavior is found for the (220) grains with a high Schmid factor of 0.47. While (220), (111) and (200) oriented grains exhibit a phase transformation, (311) grains plastically deform solely by slip. During plastic deformation a load redistribution from soft behaving (220) grains to hard behaving (200) orientated grains takes place. The presence of VC precipitates leads to a broadening of the stress interval at which a martensite transformation is induced. This is explained by spatially heterogeneously distributed martensite transformation temperatures which are caused by VC precipitates. The microstructural reason for pseudo-elasticity is found to be a combination of back transformation from hcp to fcc and a reversible motion of Shockley partial dislocations.

Keywords: FeMnSi; shape memory alloy; Neutron diffraction; Martensite

1 Introduction

Fe-Mn-Si based shape memory alloys (SMA) have been widely studied since the discovery of the shape memory effect (SME) in these alloys by Sato in 1982. They are considered to be a cost-effective alternative to expensive NiTi based alloys for technical applications, e.g. as pre-stressing elements for concrete structures in civil engineering, as clamping or coupling devices [1,2]. The SME in Fe-Mn-Si SMAs is based on the stress-induced transformation from a parent austenite fcc phase (γ) to a martensite hcp phase (ε) and its reversion (hcp to fcc) by heating. The formation of hcp martensite from the fcc austenite phase is considered to be achieved by the motion of a/6 <112> Shockley partial dislocations (SPD) on non-adjacent close-packed planes, where a is the lattice parameter [3,4]. In the past 30 years, many different alloy compositions were produced and characterized with respect to their shape memory properties [1-4]. The shape memory effect can be increased by the so-called "training" effect, i.e., repeated deformation at room temperature followed by an annealing process at 650-800 °C [5-7]. In 2001, Kajiwara et al. found that the SME can be strongly improved by producing fine precipitates of coherent NbC without any additional "training" [8-12]. This was related to the formation of large elastic strain fields in the vicinity of the precipitates, which provide preferential nucleation sites for the stress- induced transformation from the fcc to the hcp phase [11]. The precipitates are also assumed to increase the strength of the austenite and, then, effectively prevent slip deformation [5]. In other works, the influence of VC or VN [13, 14], TiC [15] as well as $Cr_{23}C_6$ [16] precipitates on the SME was investigated. Even though improved shape memory properties were reported for all these alloys containing different kinds of precipitates, Stanford and Dunne put the explanation of many studies in question [17]. They proposed that the improved SME of many studies attributed to precipitation is likely to be the result of the thermo-mechanical processing used in those experiments. A precipitate free reference material which is required to distinguish the impact of precipitates from the impact of the thermo-mechanical treatment on the SME is still missing.

FeMnSi based shape memory alloys are used for prestressing applications e.g. in civil engineering. The increase of the recovery stress, i.e. the formation of stress due to a constraint shape recovery, is highly desirable from an application point of view. Precipitates have an impact on both the strength and the SME of the material. In order to increase the recovery stress both of these properties need to

be optimized. The strength of the material describes the upper limit of the achievable recover stress. Understanding the impact of precipitates on the SME is a first step towards increasing the recovery stress in FeMnSi based shape memory alloys.

Pseudoelasticity in Fe-Mn-Si alloys has only been scarcely described previously [18-20]. The increase of pseudoelasticity depends linearly on the applied maximum stress before unloading [18]. This is an argument for a back transformation from hcp to fcc upon unloading, in Fe-Mn-Si-alloys as it has been proposed by Matsamura et al. [19]. The authors argued that the pseudoelasticity is dependent on the magnitude of the applied external stress (as has been confirmed in [18]) as well as on the stacking fault energy (SFE). At this point it is not clear what is the amount of strain caused by the back transformation from hcp to fcc and by dislocations. Due to the low stacking fault energy, stacking faults are expected to form.

X-ray and neutron diffraction provide phase selective information on various microstructural properties such as relative volume fraction of a specific phase, texture, internal stress, etc., and are therefore frequently applied to study phase transformations. When applied in-situ during deformation, it allows to follow the strain dependent evolution of the transformation [21-23]. Thermal Neutrons, as used in the present study, have a penetration depth in the range of mm to cm in pure iron. This allows studying the mechanical response of grains across the whole cross section of the specimen when compared with x-rays where the interaction volume is limited to the surface layer of the material. By probing grains within the sample, effects due to open surfaces can be ruled out and the bulk behavior is studied. Furthermore, neutron diffraction is the method of choice for separating the contribution of reversible phase fraction (integrated intensities of peaks) from the contribution of dislocation movement (change of full width at half maximum of peaks in the absence of a phase transformation) on the pseudo-elastic properties. There exists a vast amount of literature that report on in-situ mechanical testing of shape memory alloys, in particular for the NiTi system (see, for instance, [21] and references therein) and for Cu-based SMAs (see, for instance, [24] and references therein). In-situ experiments have not been yet frequently applied to study the Fe-Mn-Si system. Oliver et al. reported on an in-situ neutron diffraction study of Fe-Mn-Si SMA with and without VN precipitates [25]. It was found that the VN precipitates promote martensitic transformation; however, they also pronounce differences in the extent of

transformation between differently orientated austenite grains, leading to increased intergranular stresses. By investigating the behavior of individual hkl-diffraction peaks it was found that (220) grains transform most readily, in agreement with their high Schmid factor.

The aim of the present work is to systematically study the fcc to hcp transformation during loading and unloading in an Fe-17Mn-5Si-10Cr-4Ni(-1VC) shape memory alloy using in situ neutron diffraction. This alloy has been designed for use in civil engineering and therefore has comparably low transformation temperatures [18]. It has been studied extensively with regard to its microstructure, shape memory properties with a special emphasize on shape recovery stresses under mechanical constraints, static and cyclic materials properties and corrosion behavior [26-29]. The goals of the present study are to describe the influence of carbide precipitates on the fcc to hcp transformation for this particular master alloy composition, to study the fcc to hcp transformation as a function of the grain orientation and potentially resulting load transfers between different grain families and to shed light on the general microstructural mechanisms of pseudo-elasticity. For this, two different alloy batches with and without the addition of V and C have been prepared. The results of this study are relevant for developing strategies for the microstructural design of Fe-Mn-Si SMAs with regard to applications where either a pronounced SME or high shape recovery stresses are required.

2 Materials and Methods

For this work the iron based SMA Fe-17Mn-5Si-10Cr-4Ni was used as master alloy. Two different batches were produced: one with the targeted addition of 0.76 wt.% V and 0.21 wt.% C to produce fine carbides and one without V and a low carbon content (<0.02 wt.%). The alloys were prepared in form of plates that were produced following the same procedure as described in [18]. First, two batches of approximately 20 kg were cast into cylindrical molds (Ø 160 mm) under atmospheric conditions. The chemical compositions as measured by optical emission spectroscopy are listed in Table 1. Then, both alloys were hot forged at 1150°C to a rectangular bar with a cross section of 100 × 100 mm. After the forging, plates with final dimensions of 20 × 100 × 800 mm were produced in several steps of hot rolling at 1150°C. Finally, the alloys underwent different heat treatments. Table 1 summarizes the different processing steps for the investigated alloys. The microstructure of the investigated alloys is

shown in Figure 1. SMA7 has the smallest grains, followed by SMA1 and SMA7-2. SMA1 aged shows precipitates on the grain boundaries and within grains as expected due to the aging treatment. In SMA7-2 the grains are comparably large with diameters of several 100 μm.

Alloy	Fe	C	Mn	Si	Cr	Ni	V
Target		0.21	17.00	5.00	10.00	4.00	0.76
SMA1	Bal.	0.18	17.17	5.06	9.99	4.21	0.74
SMA7	Bal.	0.009	17.05	5.04	10.07	4.15	---

Table 1: Chemical composition of master alloys according to optical emission spectroscopy measurements

Chemical composition [wt. %]	Hot rolling temperature	Solution treatment	Precipitation treatment	Designation	Experiment
Fe-17Mn-5Si-10Cr-5Ni-1VC	1150°C	1100°C/2h	850°C/2h	SMA1 aged	Monotonic tensile test
Fe-17Mn-5Si-10Cr-5Ni	1150°C	-	-	SMA7	Monotonic tensile test
Fe-17Mn-5Si-10Cr-5Ni	1150°C	1100°C/2h	-	SMA7-2	Cyclic tensile test

Table 2: Chemical composition and thermal treatments of monotonic and cyclic tensile tested samples
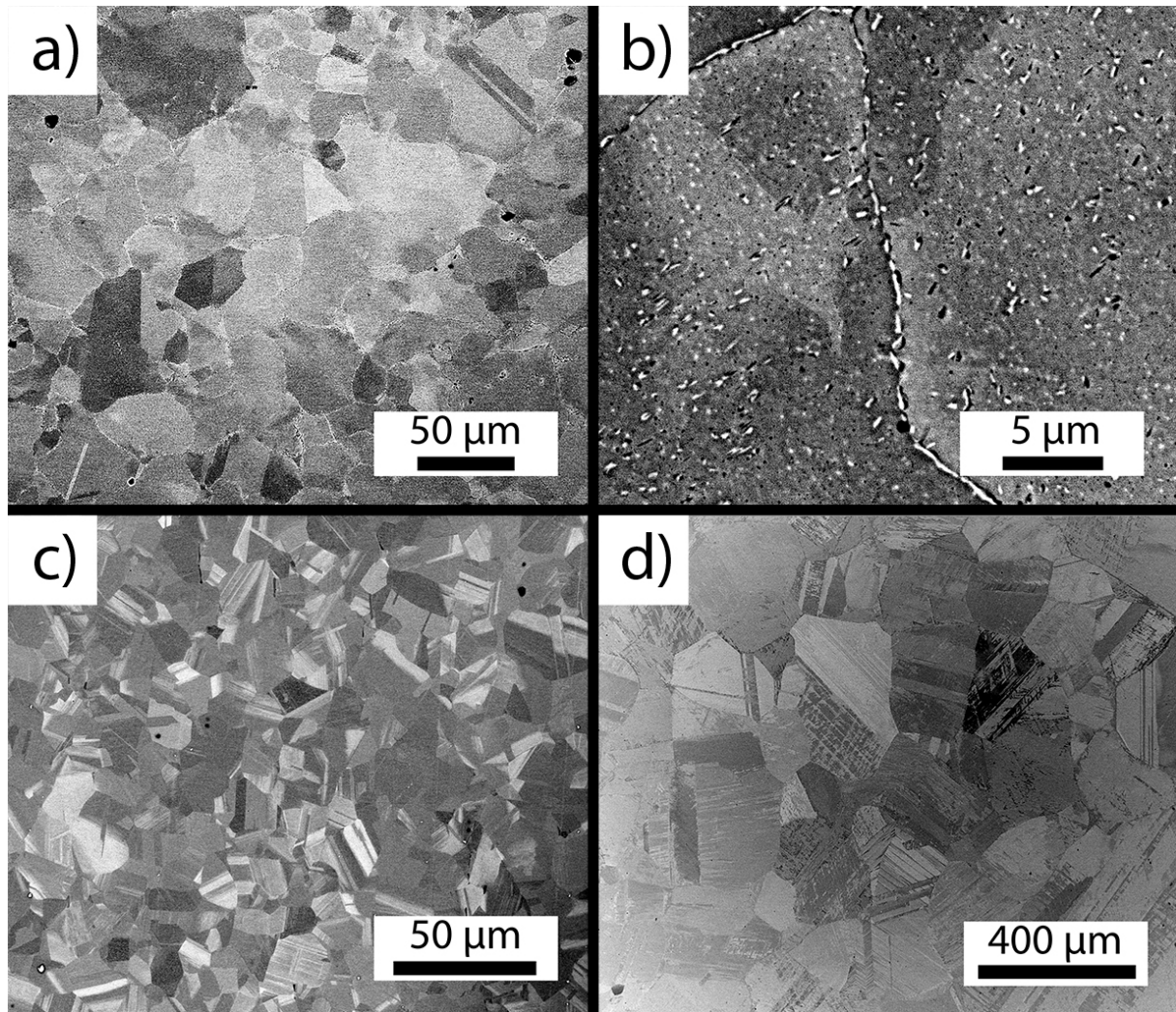
Figure 1: SEM backscattered electron micrographs of a) SMA1 aged, b) detail view of SMA1 aged showing a grain boundary and precipitates, c) SMA7 and d) SMA7-2

Round tensile samples with a diameter of 6 mm and a gauge length of 25 mm were machined from the plates. A clip-on extensometer was directly mounted on the sample. In situ neutron diffraction experiments were performed at the time-of-flight (TOF) strain scanner POLDI at the continuous Swiss Spallation Neutron Source with an incident neutron beam of wavelength range of 1.1–5 Å (Please see [30] for a detailed review of the setup).
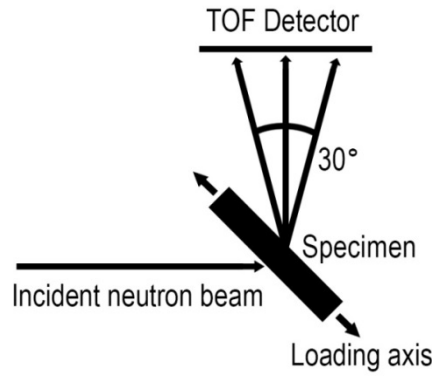
Figure 2: Measurement setup of neutron diffraction during uniaxial loading. Planes which have their normal vector parallel to the loading direction fulfill the Bragg condition.

The instrument has one detector bank, which is centered on a horizontal scattering angle of 90°. The 30 kN stress rig used in this experiment was placed as showin in Figure 2. In this configuration hkl lattice planes which have their hkl plane vector parallel to the loading axis fulfill the Bragg condition (axial alignment). A one-dimensional position sensitive detector is used to collect neutrons under an opening angle of 30° as shown in Figure 2. At each stress stage the measurement period of the diffraction pattern was 120 min. The macroscopic strain was measured using an extensometer for all tests. Interrupted quasistatic tensile tests were performed with the samples SMA1 aged and SMA7 to study the influence of carbide precipitates on the stress-induced fcc to hcp transformation. Here a maximum strain of 10 % was applied. Cyclic tensile tests with increasing maximum strains of 1.0 %, 3.3 % and 8.9 % and intermediate unloading to 0 N were performed with the sample SMA7-2 to investigate the mechanisms of pseudo-elasticity more precisely. The diffraction peaks are fitted using the multi-peak fitting routine available at POLDI with Gaussian functions. During the measurement intervals, the displacement was kept constant, yielding some stress relaxation, and neutron acquisition has been started after three minutes relaxation time.

The fcc peaks (220), (111), (200) and (311) of the alloy SMA1 aged, SMA7 and SMA7-2 were quantified by analyzing the Gaussian integrated intensity and the full width at half maximum (FWHM). Using the Bragg equation the average interplanar lattice spacing d_{hkl} for an hkl grain family is obtained. The lattice strains were calculated according to:

$$\varepsilon_{hkl}(\sigma_T) = \frac{d_{hkl}(\sigma_T) - d_{0hkl}}{d_{0hkl}} \qquad (1)$$

where d_{0hkl} denotes the lattice spacing before loading and σ_T the applied true stress.

3 Results
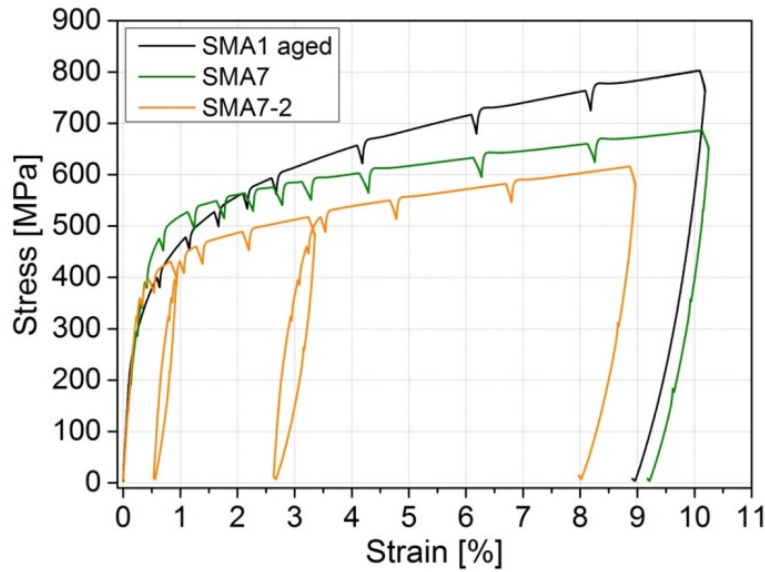
3.1 Macroscopic stress strain behavior

Figure 3: Stress strain characteristics for SMA1 aged, SMA7 and SMA7-2 recorded during interrupted in-situ neutron diffraction measurements

	SMA1 aged	SMA7	SMA7-2
$\sigma_{y0.1}$ [MPa]	305	340	370
$\sigma_{y0.2}$ [MPa]	350	415	390

Table 3: Yield strengths of SMA1 aged, SMA7 and SMA7-2

Figure 3 shows the macroscopic stress strain response during the interrupted tensile test for the three batches of SMAs. The spikes are caused by a stress relaxation as mentioned above. The 0.1% and 0.2% yield stresses in Table 2 have to be understood as approximate values due to relaxation phenomena taking place in the material as described above. These relaxation phenomena shift the stress strain curves and make a precise determination of the yield not possible. The precipitate containing material, SMA1 aged, has the lowest yield for both $\sigma_{y0.1}$ (305 MPa) and $\sigma_{y0.2}$ (350 MPa). Besides, the most pronounced hardening is observed in SMA1 aged. Compared to SMA1 aged, the alloys SMA7 and SMA7-2 have similar stress strain characteristics while the onset of plastic deformation in SMA7 is shifted to a higher stress. The stress strain curves reveal that SMA7 has a higher strength than SMA7-

2. For SMA7-2 (cyclic testing) the evolution of the stress strain curve shows a continuous envelope. The hardening characteristics of the second and third cycle follow those of the corresponding previous cycle. Pseudo-elasticity, i.e. an additional fraction of non-linear strain recovery, is observed for all three batches of SMAs during unloading.

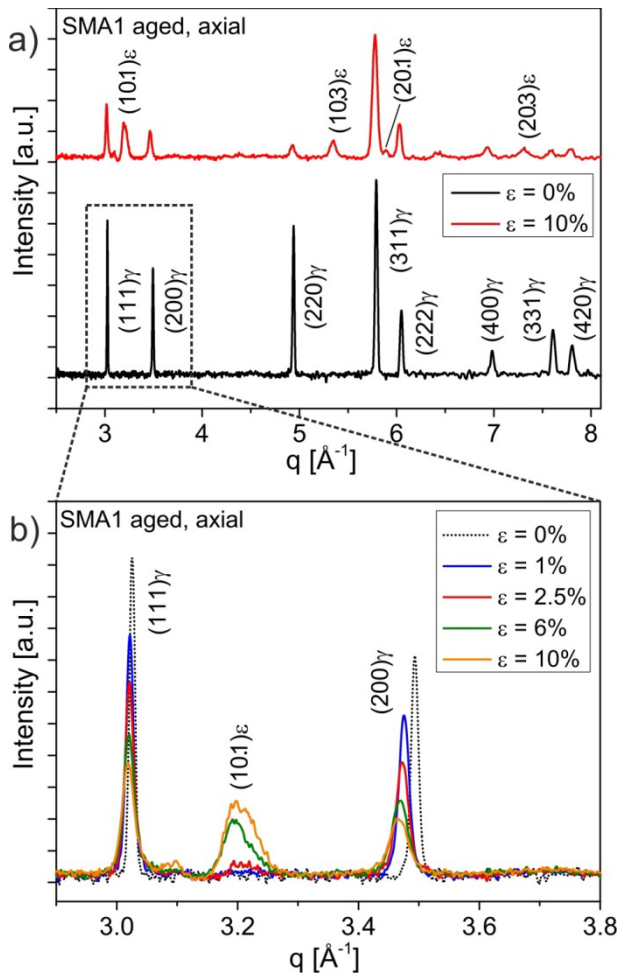3.2 In-situ neutron diffraction during monotonic tensile tests

Figure 4: a) Full axial neutron diffraction spectra from samples in the undeformed state and after straining to 10 %, b) diffraction spectra in selected q-regime for step-wise increase of strain from 0 % until 10 %

Figure 4 a) shows exemplarily two diffraction spectra for SMA1 aged at 0 % and 10 % total strain. Very similar spectra were measured for the two other batches. While only diffraction peaks of the austenite phase appear in the unloaded state, additional peaks appear when the sample is strained to 10%

which can be assigned to hcp martensite. A selected region of q-spacing between 2.9 Å^{-1} and 3.8 Å^{-1} is magnified in Figure 4 b) for different deformation states between 0% and 10%. The integrated intensities of the (111) and (200) austenite peaks decrease. A shift of the peak positions towards smaller q-values and a peak broadening is observed with increasing load. The hcp martensite peak for the (10.1) grain family appears after straining the sample to 2.5 % and its intensity increases thereafter with increasing strain. As expected, the hcp peak is broader and noisier compared to the fcc peaks.
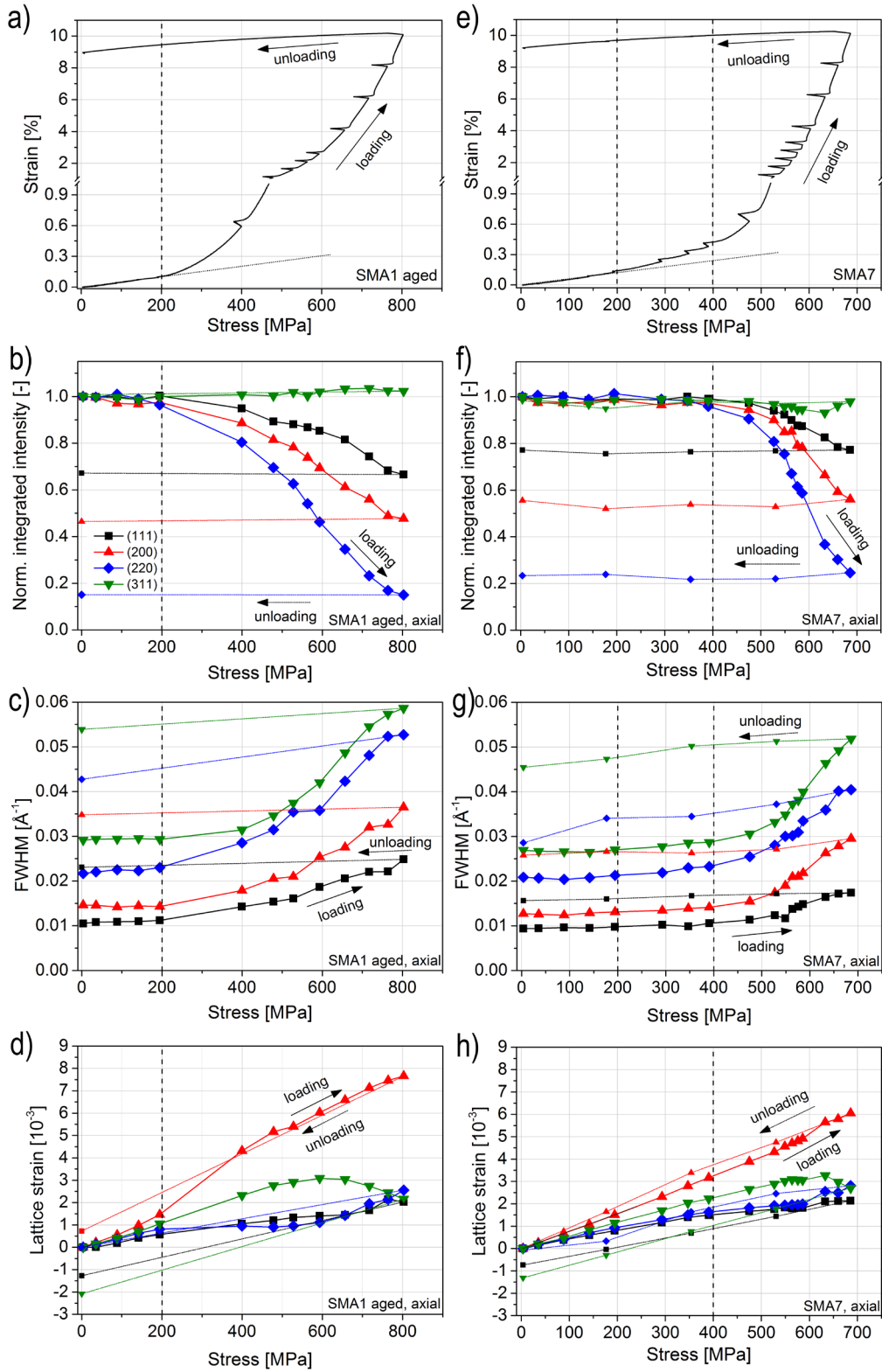
Figure 5: Strain stress curve during interrupted quasistatic tensile test in a) and e), plots of normalized integrated intensity over stress in b) and f), plots of FWHM over stress in c) and g), plots of lattice strain as a function of stress in d) and h) for SMA1 aged and SMA7, respectively, capturing austenitic (111), (200), (220) and (311) grain families in axial alignment

In Figure 5, the normalized integrated peak intensities, the full widths at half peak maximum (FWHM) and the lattice strains are plotted as a function of applied stress for the (111), (200), (220) and (311) grain families of SMA 1 aged and SMA7 and compared to the strain stress curves of the two alloys. The integrated intensities of SMA1 aged shown in Figure 5 b) do hardly change up to a stress of 195 MPa. For higher stresses a continuous decrease of the integrated intensities for the (220), (200) and (111) grains is observed. The decrease of the integrated intensity at the maximal applied load of around 800 MPa strongly depends on the grain orientation. The (220) grains reveal the most pronounced intensity decrease by 85% while the intensity only decreases by 53% and 33% for (111) and (200), respectively. In contrast to these three other grain families the integrated intensity of the (311) grains remains at almost 100 % independent of the externally applied stress.

SMA7 shows qualitatively a similar behavior but the onset of the integrated intensity decrease is shifted to a higher stress. At 400 MPa the normalized integrated intensity starts to decrease for SMA7. As in the case of SMA1 aged the maximum intensity drop at the final stress of 690 MPa depends on the grain orientation for SMA7. Again, (220) grains show the largest decrease of normalized integrated intensity of 75%, followed by (200) grains with 44 % and (111) grains with 23 %, i.e. for SMA1 aged and SMA7 the integrated intensity decreases most for the (220) grains followed by (200) and (111) grains. The onset of the intensity decrease of (220), (200) and (111) grains at 400 MPa for SMA7 corresponds to the 0.2% yield point of the material of 415 MPa. The integrated intensities of the individual grain families of SMA1 aged and SMA7 decrease with different rates. For SMA7 this rate is higher for every grain family compared with SMA1 aged. It is remarkable that a similar total intensity decrease at 690 MPa is attained when the same grain orientations of SMA1 aged and SMA7 are compared. After unloading, the integrated intensities remain on the same level determined as at maximal load for both materials SMA1 aged and SMA7.

The evolution of FWHM as a function of the applied stress is plotted in Figure 5 c) and g). The FWHM of SMA1 aged remains constant until the yield point at 195 MPa and then starts to increase non-linearly. At stresses larger than 195 MPa a linear increase of FWHM is observed for SMA7 followed by a pronounced non-linear increase of FWHM after 400 MPa. Thus the onset of a pronounced increase of FWHM is 205 MPa higher for SMA7 when compared with SMA1 aged as already ob-

served for decreasing integrated intensities. After unloading the FWHM of both materials decreases slightly for all four grain orientations.

The lattice strains for SMA1 aged and SMA7 shown in Figure 5 d) and h) increase linearly for all austenite phase grain families until the yield stress is reached. For SMA1 aged the slope of the micro-strain stress curve of the (220) grains starts decreasing at the yield point of 195 MPa. A similar but less strong decrease is observed for the (111) grains at 195 MPa and for the (311) grains at a higher stress of 400 MPa. The (200) grains behave in an opposite way. For these grains an increased slope of the micro-strain stress curves is observed starting at 195 MPa. At 600 MPa the slope of the (220) and (111) grains increase. At the same stress level the integrated intensities and the FWHM of the (220), (111) and (200) grains show an inflection point. In addition, the slope of the micro-strain stress curve of the (311) grains becomes negative. A qualitatively similar behavior is observed for SMA7. The difference to SMA1 aged is that the slope changes are less pronounced and significant changes of the micro-strains are shifted to higher stress values of 400 MPa.

3.4 In-situ neutron diffraction during cyclic tensile testing

Cyclic tensile tests, i.e. tensile tests with three loading and unloading cycles with increasing maximum strains of 1.0 %, 3.3 % and 8.9 %, were performed with the sample SMA7-2. The aim was to study in detail the structural changes that lead to the nonlinear, pseudo-elastic behavior of the alloy. The yield is marked in all plots of Figure 6 by a dotted line. The (220) and (200) grains show a dissimilar strain stress behavior during monotonic tensile tests. While in some regions the strain is independent of stress for the (220) directions, the (200) grains show a strain increase beyond what is expected from linear elastic behavior. As will be later discussed, (220) grains behave soft while (200) grains behave hard during plastic deformation. For this reason we study (220) and (200) grains as representatives of soft and hard behaving grains for the analysis of pseudo-elasticity. For both grain orientations integrated intensities, FWHM and lattice strain were derived from the diffraction data. The pseudo-elasticity ε_{pe}, which is defined as the non-linear strain fraction after unloading, is given as

$$\varepsilon_{pe,i} = \left[\Delta\varepsilon_{t,i} - \varepsilon_{el,i}\right] \cdot 100\% = \left[\left[\varepsilon_{max,i} - \varepsilon_{min,i}\right] - \frac{\sigma_{max,i}}{E}\right] \cdot 100\% \qquad \text{(with i = 1, 2, 3) (Eq. 2)}$$

where $\Delta\varepsilon_{t,i}$ is the total strain difference between maximal loading and unloading ($\varepsilon_{max,i}$ and $\varepsilon_{min,i}$), $\varepsilon_{el,i}$ is the elastic spring back, σ_{max} is the maximal applied stress in the corresponding loading cycle and E is Young's modulus. The lowest pseudo-elasticity of 0.15 % appears after the first loading cycle followed by 0.41 % and 0.62 % after the second and third cycle, respectively.

At the yield stress the integrated intensity of the (220) grains starts to decrease during the first cycle while the integrated intensity of the (200) grains almost does not change as seen in Figure 5 b) and e). During the second and third cycle the integrated intensities of the (220) and (200) grains decrease gradually. After unloading the integrated intensity increases by 6 %, 4 % and 1 % after the first, second and third cycle for the (220) grains. For the (200) grains an intensity increase of 4 % and 2 % is observed after the second and third cycle.

The FWHM shown in Figure 6 c) and f) increases at the yield of 320 MPa for the (220) and (200) grains. It increases stepwise when the strain is increased to 3.3 % and 8.9 % during cycles two and three, respectively. When the sample is unloaded a decrease of FWHM is observed for both grains (220) and (200). The highest decrease of FWHM is observed after unloading from the third cycle. Here a decrease of 0.014 Å^{-1} for the (220) grains and of 0.004 Å^{-1} for the (200) grains is observed.

The lattice strain of the (220) grains shown in Figure 6 d) increases linearly up to the yield stress during the first cycle and slightly decreases with further loading. A compressive strain of -0.7 % remains after unloading. A qualitatively similar behavior is observed for the second cycle with an increased residual compressive strain of -0.9 %. During the third cycle the lattice strain increases linearly with strain and the before mentioned decrease of strain during loading for cycles two and three is absent. A compressive strain of -1.1 % is observed after unloading. For the (200) grains the micro-strain stress curve is almost linear for all three cycles. A residual compressive strain of -0.2 % is observed after the second and third cycle.
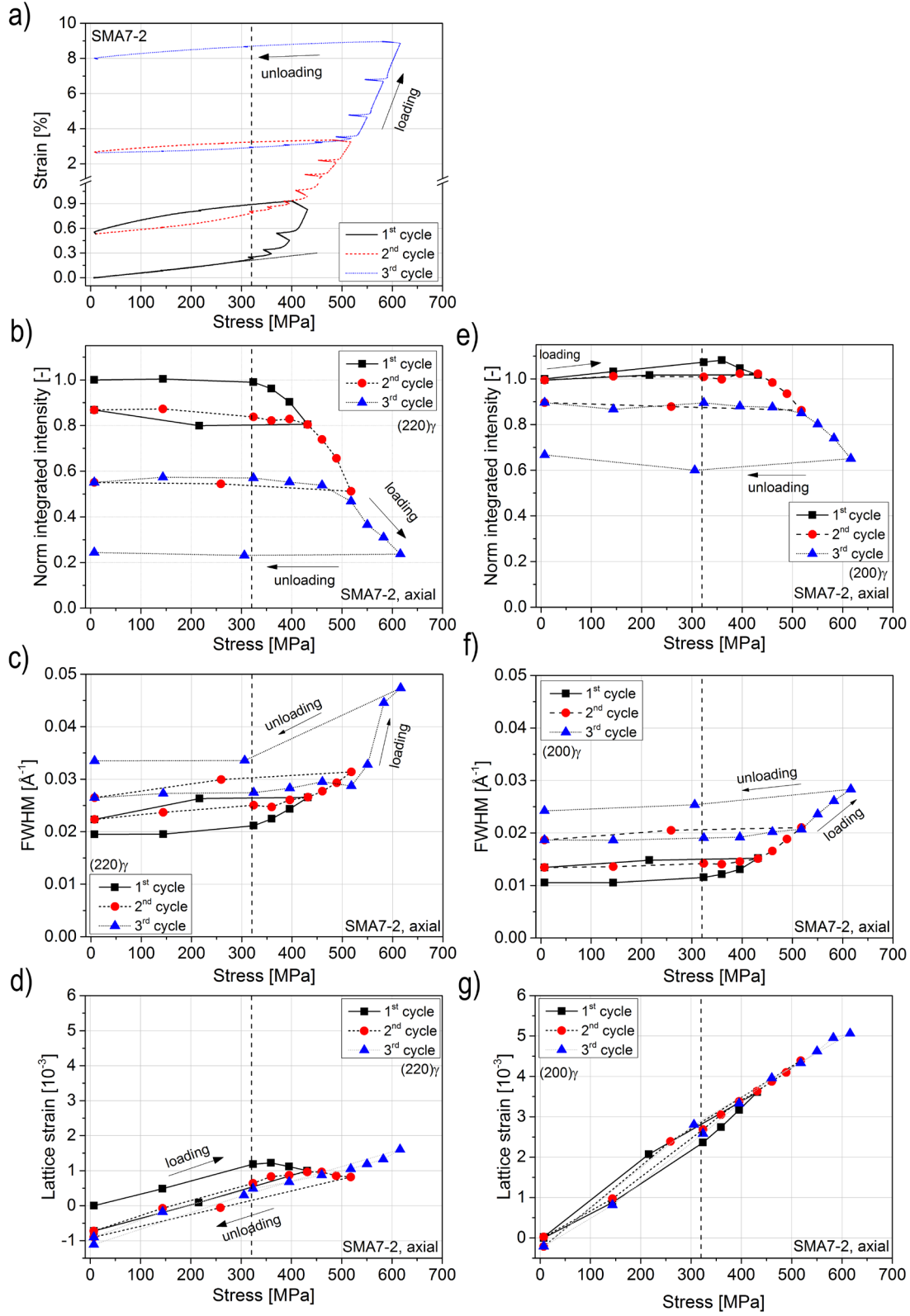
Figure 6: a) Strain stress curve from interrupted cyclic test, b) and e) plot of normalized integrated intensity over stress, c) and f) plot of FWHM over stress and d) and g) plot of lattice strain over stress for the austenitic (220) and (200) grain orientations within SMA7-2.

4. Discussion

4.1. Influence of VC precipitates on the formation of hcp martensite

For SMA1 aged and SMA7 the deviation from a linear macroscopic stress strain behavior is correlated with a decrease of the integrated intensities of the (220), (111) and (200) austenite grain families. Considering the peak intensity as a measure for the volume fraction of a phase in a certain grain orientation within the sample and neglecting grain rotation, the decrease of the fcc peak intensities must be assigned to the transformation from fcc austenite to hcp martensite. Consequently, it can be claimed that the transition towards non-linear stress strain behavior in the batches SMA1 aged and SMA7 is caused by the formation of hcp martensite. The beginning of the hcp transformation is shifted to lower stresses and the rate at which martensite forms for any grain family is reduced when VC precipitates are present. The onset of hcp martensite transformation at lower stresses in SMA1 aged compared to SMA7 and SMA7-2 is the reason for the increased strain hardening rate of SMA1 aged as observed in the macroscopic stress strain curves. This hardening can be explained by the interaction of differently aligned martensite variants or by the interaction of martensite plate tips with grain boundaries or precipitates [31, 32]. This suggests that the yield stress for the martensite transformation in SMA1 aged is lower than in SMA7. This assumption will be proven in the following discussion by the analysis of integrated intensities of individual peak families. When comparing the two materials without precipitates, i.e. SMA7 and SMA7-2, the stress strain curves in Figure 2 reveal an increased strength for SMA7. We attribute this strengthening to a Hall-Petch effect since the grain size of SMA7 is smaller than the grain size of SMA7-2 as observed in Figure 1c) and 1d).

Precipitates in the austenite matrix are responsible for the reduction of stress at which the hcp transformation is observed. When coherent or semi-coherent precipitates are formed at elevated temperatures stress fields are created due to the mismatch of lattice constants. During cooling it can be assumed that precipitates and the matrix material have different thermal coefficients which will lead to thermal stresses during cooling. Therefor we assume stress fields in the vicinity of precipitates. These stress fields have an impact on the martensite phase transformation temperature. Stresses shift the phase transformation temperature towards higher temperatures according to the Clausius-Clapeyron equation and thus facilitate the formation of stress-induced martensite [33, 34]. Due to the spatial het-

erogeneity of stresses within the VC precipitate containing material, the local martensite transformation temperature will spatially vary. In some regions martensite preferentially grows at a given stress while in other regions the transformation is delayed because higher stresses are required to induce the hcp phase. In contrast SMA7 is expected to show more homogeneous spatial phase transformation temperatures due to the absence of precipitates. For this reason the integrated intensities of SMA1 aged decrease slowly over a wider stress period of 195 MPa to 800 MPa when compared to the pronounced decrease of integrated intensities of SMA7 within a narrow stress range between 400 MPa and 690 MPa.

The fcc to hcp transformation is caused by the movement of SPDs on every second layer [2]. These dislocations will distort the fcc lattice. Especially at the tip of hcp martensite plates a high distortion of the austenite matrix is expected. For this reason the increase of FWHM as a measure of elastic strain gradients is correlated with the decrease of integrated intensities, i.e. with the fcc to hcp transformation in (220), (111) and (200) grains. While for SMA1 aged the decrease of integrated intensity and an increase of FWHM are simultaneously observed at 195 MPa, for SMA7 an increase of FWHM is observed at 195 MPa and a delayed decrease of integrated intensity at 400 MPa. This increase of FWHM in the absence of a decrease of integrated intensities in SMA7 in the interval of 195 MPa to 400 MPa can be explained by the formation of dislocations, preferentially SPDs. SPDs are assumed to be nucleation sites at stresses of 400 MPa for hcp martensite. The role of full dislocations and SPDs will be discussed in the following section.

When carefully comparing the FWHM of individual grain families between SMA1 aged and SMA7 prior to loading it is noticeable that the FWHM of every grain family of SMA1 aged are slightly higher than the ones of SMA7. Thus SMA1 aged shows higher elastic strain gradients in the unloaded state than SMA7. This increase of elastic strain gradients in the unloaded state of SMA1 aged can be explained by an increased amount of dislocations, preferentially SPDs, and by lattice strains due to precipitates. At around 400 MPa the FWHM of the different grains of SMA7 increased to the same magnitude as those of SMA1 aged in the unloaded state. This observation agrees well with the reduction of the necessary stress of 205 MPa to observe a fcc to hcp transformation when comparing SMA1 aged with SMA7.

4.2 Mechanical anisotropy and martensite texture

As the only grain family the (311) grains do not show any changes in integrated intensity. As explained above, a change of integrated intensity indicates a phase transformation. Thus the (311) grains remain in the fcc phase independent of the applied stress. The FWHM of the (311) grains increase for both SMA1 aged and SMA7 during loading. Twinning leads to a rearrangement of grain orientations. In that case a decrease of integrated intensities would be expected but is not observed for the (311) grains. Therefore we can exclude twinning of (311) grains. We assume that slip occurs in (311) grains since slip does not change the integrated intensities but will increase the FWHM as observed. The main shear system for slip in fcc crystals is {111}<110> which differs from the shear system of the fcc to hcp phase transformation {111}<112>. The Schmid factor determines whether a grain orientation is more prone to phase transformation or to slip. The unidirectionality of the shear system {111}<112> for the phase transformation must be considered when calculating the corresponding Schmid factors [35, 36]. This unidirectionality caused different Schmid factors when straining the material under compression or tension. The Schmid factor related to the slip deformation is 0.45 for the (311) grains and is thus higher than the Schmid factor related to the fcc to hcp transformation of 0.39. This fact supports the assumption of slip as the deformation mode rather than a phase transformation. The grain orientation dependent Schmid factors for phase transformation and for slip are summarized in Table 3.

Grain Family	Schmid factor phase transformation {111}<112>	Schmid factor slip {111}<110>	E modulus SMA1 aged	E modulus SMA7
(200)	0.24	0.41	145	131
(311)	0.39	0.45	202	172
(220)	0.47	0.41	226	202
(111)	0.31	0.27	340	237

Table 4: Grain orientation dependent Schmid factors for phase transformation and slip, elastic moduli for SMA1 aged and SMA7.

The orientation relationship between fcc and hcp is given by Shoji-Nishiyama. There exist in total four hcp variants which are differently orientated in space. Since the Schmid factor determines which hcp variants preferably form, a martensite texture formation is expected. At first sight it seems as if hcp variants preferentially form which have their (10.1) planes normal to the loading axis for SMA1 aged and SMA7 as observed from the strong growth of the hcp (10.1) peak in the neutron diffraction spectra. The observed hcp (10.1) peaks have their (00.1) planes tilted by 62° against the loading axis. The Schmid factor for a fcc to hcp phase transformation under 62° is at most 0.33 and thus small when compared to the maximum Schmid factor of 0.50. For this reason the hcp (10.1) peak does not appear at that stress at which the intensities of the austenite peaks decrease (195 MPa for SMA1 aged) but at a much higher stress (600 MPa, 2.5 % macroscopic strain, for SMA1 aged). Thus it can be assumed that the hcp variants which have the (10.1) planes normal to the loading axis do not constitute the main martensite texture components. According to the Shoji-Nishiyama orientation relation the hcp (00.1) planes are parallel to the fcc (111) planes which are the planes of shear. At a tilting angle of 45° against the loading direction the Schmid factor is maximal and thus hcp variants with (00.1) planes tilted by 45° against the loading direction are expected to be the main martensite texture components.

These variants are expected to form at 195 MPa for SMA1 aged but will not show any peaks in the neutron diffraction spectra because they do not exhibit low indexed lattice planes which are normally orientated to the loading direction as obtained from pole figure simulations.

For the analysis of strain stress curves obtained from neutron diffraction data it is important to keep in mind that a change of strain of a specific grain family is caused by a change of stress acting on this specific grain family (Figure 5 d) and h)). These strains are micro-strains and are derived from the peak positions according to Equation 1. Changes of intergranular and intragranular stresses will change the micro-strains. The former are expected to play a role when grain families start to behave plastically. For the present material the growth of hcp martensite within the austenite matrix is not stress free and might therefore cause intragranular stresses. Dislocations at the tips of the martensite plates might influence micro-strains of the surrounding austenite matrix. However peak position changes due to intragranular stresses were not identified during the analysis of micro-strain stress curves. When the micro-strain within a grain family does not change with increasing external stresses (horizontal line in micro-strain stress diagram) this grain family is behaving perfectly plastic. Additional stresses acting on these grains will completely relax by a fcc to hcp transformation. This phenomenon is observed for the (220) grains of SMA1 aged in the stress interval of 195 MPa to 400 MPa. In this range the (220) grains cannot carry any additional load. For SMA7 no horizontal lines in the strain stress curves are observed but as for SMA1 aged the (220) grains start to behave elastically soft at around 400 MPa. For SMA1 aged and SMA7 the integrated intensities of the (220) grains show the largest decrease. We attribute the soft behavior of the (220) grains to a preferential phase transformation. This assumption is in accordance with the very high Schmid factor of 0.47. In the case of (200) grains the Schmid factor for slip of 0.41 is larger than for the phase transformation of 0.24. Thus we assume that a deformation mode is slip for (200) orientated grains. However the integrated intensity of (200) orientated grains starts to decrease at 195 MPa. Therefore a combination of slip and phase transformation is expected for (200) orientated grains. (200) grains are identified as hard grains from the increase of the slope of the micro-strain stress curve in the plastic regime contrary to the behavior of (220) oriented grains. The interaction of slip and hcp bands or the interaction of hcp bands of different hcp variants aligned shear systems is expected to cause the hard behavior of (200) grains. The in-

teraction of differently hcp variants is known to cause strain hardening in FeMnSi-based single crystals which are strained along the <001> axis [32]. Since (200) grains behave hard and (220) grains behave soft we conclude a load transfer from (220) to (200) grains in the plastic regime. The (111) grains have a small Schmid factor of 0.31 for the phase transformation which is still larger than the Schmid factor for slip of 0.27. The decrease of integrated intensities is caused by a phase transformation in these grains. The (111) grains show a softening behavior, though the plasticity is not as perfect as in the case of the (220) grains. The (111) grains therefor still carry small amounts of additional load in the plastic regime starting at 195 MPa in SMA1 aged and at 400 MPa for SMA7.

It is assumed that (311) grains are plastically straining to a larger extent than the surrounding grains. For this reason (311) grains are compressively stressed starting at 600 MPa for SMA1 aged and at 630 MPa for SMA7. These compressive stresses result in a negative slope in the strain stress curves of the (311) grains as show in Figure 5 d) and h). The same argument applies to the (220) grains of SMA7-2 which show a negative strain stress slope at 360 MPa during cycle one in Figure 6 d). After unloading compressive strains remain in (111) and (311) grains for SMA1 aged and SMA7. These compressive strains arise because the surrounding grains will elongate to a larger extent after unloading. (111) and (311) grains exhibit comparatively small elastic (back) strains due to a pronounced irreversible plastic deformation. Surprisingly (220) grains do not contain compressive strains after unloading though they showed the most pronounced plastic behavior. For the (220) grains, the integrated intensity does not change during unloading but the FWHM decreases which we attribute to the reversible motion of SPDs. Thus a part of the plasticity in (220) is actual pseudo-elasticity. Due to this pseudo-elastic behavior of (220) grains no compressive stresses remain after unloading.

The critically resolved shear stress (CRSS) is a material constant and describes the required shear stress acting on the appropriate shear system in order to observe a shear deformation. It is given by

$$\text{CRSS} = E \times \varepsilon \times S \tag{3}$$

where E is the elastic modulus of the grain family, ε is the micro-strain and S is the Schmid factor of the grain family. Plasticity in SMA1 aged and SMA7 is mainly governed by a fcc to hcp phase transformation which can be understood as a shear deformation. To determine the CRSS for SMA1 aged and SMA7 grain orientation elastic moduli were calculated by using Hook's law. For the calculation

the linear elastic micro-strain stress curves shown in Figure 5 d) and h) up to a maximum stress of 150 MPa were considered. As shown in Table 3 both SMA1 aged and SMA7 show a cubic elastic anisotropy for the four investigated grain orientations (200), (111), (220) and (311). The dense [(111)] directions show the highest elastic moduli while along [(200)] the lowest elastic moduli are observed. SMA1 aged shows higher elastic moduli for all grain families when compared to SMA7. This increase is assumed to be caused by the VC precipitates which have a comparatively high elastic modulus in the range of 380 GPa [37]. Additionally dissolved V and C in the austenitic matrix material of SMA1 aged will have an impact on the lattice constant and alter the elastic properties of SMA1 aged compared to SMA7.

The CRSS is calculated from the lowest stress at which the fcc to hcp transformation is observed. At 195 MPa the integrated intensity of the (220) grains of SMA1 aged starts to decrease while at the same time these grains start to behave perfectly plastic, which is attributed to a fcc to hcp transformation. The $CRSS_{SMA1}$ of SMA1 aged for the (220) grains is calculated to be 85 MPa ($E_{(220)} = 226$ GPa is the elastic modulus, $\varepsilon = 0.0008$ is the strain at 195 MPa and S = 0.47 is the Schmid factor). For SMA7 the integrated intensity of the (220) grains starts to decrease at 400 MPa. At this stress a strain of 0.0016 is observed. Considering the Schmid factor of 0.47 and an elastic modulus of 202 GPa a $CRSS_{SMA7}$ for SMA7 of 152 MPa is calculated. The $CRSS_{SMA7}$ is 67 MPa higher than $CRSS_{SMA1}$. The origin of this difference are the precipitates which, as described above, lead to an increase of martensite start transformation temperature. When the martensite start transformation temperature increases lower stresses are needed to stress-induce the fcc to hcp transformation. For this reason the CRSS is shifted to lower stresses when precipitates are present.

4.3. Pseudo-elasticity

The analysis of the neutron diffraction data from the cyclic tensile test on SMA7-2 provides information about the mechanism of pseudo-elastic strain (Figure 6). As in the case of SMA1 aged and SMA7 the onset of plastic deformation for SMA7-2 is marked by a decrease of integrated intensity of the (220) grains. This decrease is associated with a fcc to hcp transformation as described above.

The pseudo-elasticity increases with increasing loading cycles, i.e. with increasing maximum strain. During unloading a back transformation from hcp to fcc takes place after each cycle for (220) grains and after the second and third cycle for the (200) grains as concluded from the growth of integrated intensities. Therefore we can associate the pseudo-elastic effect with an hcp to fcc back transformation. Since pseudo-elasticity increases with increasing strain but the amount of back transformation from hcp to fcc decreases with increasing strain, the phase transformation only partly explains the pseudo-elasticity. The FWHM of (220) and (200) grains decreases when the sample is unloaded. The decrease is more pronounced for increased total strains. This effect is strongest for the (220) grains and the (200) grains after the third cycle where the lowest increase of integrated intensity is observed after unloading. This decrease of FWHM can be explained by the reversible motion of SPDs. It is concluded that the pseudo-elastic effect is caused by a combination of a back transformation from hcp to fcc and by the reversible motion of SPDs for low strains of up to 4 % while at high strains of 8.9 % pseudo-elasticity is mainly governed by SPDs. The latter conclusion is in agreement with the observations of FWHM and integrated intensities after unloading during monotonic tensile tests of SMA1 aged and SMA7. For both materials the FWHM of all grains decreases upon unloading. Since the integrated intensity does not change after unloading from around 10 % strain (similar to the 8.9% maximum strain during cyclic tests), the decrease of FWHM seems not to be caused by a back transformation from hcp to fcc. Instead, as concluded from cyclic tensile tests, for high strains mobile SPDs which affect FWHM mainly explain the pseudo-elastic effect.

5. Summary and conclusions

Neutron diffraction measurements were performed on FeMnSi-based SMAs with and without VC precipitates in interrupted quasistatic tensile tests to track and characterize the fcc↔hcp transformations in (220), (111), (311) and (200) grain families and to study the microstructural mechanisms of pseudo-elasticity. Grain orientations (111) and (220) with a higher Schmid factor for the phase transformation than for slip showed a soft behavior in the plastic regime. A load transfer from soft behaving (111) and (220) grains to hard behaving (200) grains was observed. Deformation of (311) orientated grains is governed by slip and not by a phase transformation. This observation is in agreement with the higher Schmid factor for slip of 0.45 than for phase transformation of 0.39. The presence of VC precipitates shifts the material's yield point and the initiation of hcp-martensite down to a lower stress. The CRSS decreased from 152 MPa to 85 MPa for VC precipitate containing SMA. VC precipitates create a heterogeneous stress distribution within the material. This leads to a broadening of the stress interval at which a fcc to hcp transformation is observed when compared with the precipitate free material. The FWHM is correlated with the decrease of integrated intensity and thus with the amount of fcc to hcp phase transformation. In addition the FWHM contains information about SPDs which do not alter the integrated intensity. Pseudo-elasticity is caused by both a back transformation from hcp to fcc and by the reversible motion of SPDs. For large macroscopic strains of around 8.9 % pseudo-elasticity is solely caused by the reversible motion of SPDs.

The onset of stress-induced martensite transformation can be shifted to a lower stress according to the applications needs by using VC precipitates. For certain applications tuning the fraction of soft to hard behaving grains might be advantageous. This can be achieved by changing the texture of the poly crystal. The grain orientation dependent elastic moduli and the CRSS for the phase transformation can be employed for the simulation of mechanical behavior of poly and single crystals.

References

[1] H. Otsuka, H. Yamda, H. Tanahashi, Effects of alloying additions on Fe-Mn-Si shape memory alloys, Material Science Forum. 56 (1990).

[2] A. Sato, T. Mori, Development of a shape memory alloy Fe–Mn–Si, Mater. Sci. Eng. A. 146 (1991).

[3] L.J. Rong, D.H. Ping, Y.Y. Li, C.X. Shi, Improvement of shape memory effect in Fe-Mn-Si alloy by Cr and Ni addition, Scripta Metall. Mater. 32 (1995).

[4] H. Inagaki, Z. Metallkd. 83 (1992) 90.

[5] S. Kajiwara, Characteristic features of shape memory effect and related transformation behavior in Fe-based alloys, Mater. Sci. Eng. A. 67 (1999) 273-275.

[6] H. Li, D.P. Dunne, N. Kennon, Factors influencing shape memory effect and phase transformation behaviour of Fe–Mn–Si based shape memory alloys, Mater. Sci. Eng. A. 517 (1999) 273-275.

[7] N. Stanford, D.P. Dunne, Thermo-mechanical processing and the shape memory effect in an Fe–Mn–Si-based shape memory alloy, Mater. Sci. Eng. A. 325 (2006).

[8] A. Baruj, T. Kikuchi, S. Kajiwara, N. Shinya, Effect of pre-deformation of austenite on shape memory properties in Fe-Mn-Si-based alloys containing Nb and C, Mat. Trans. 43 (2002).

[9] A. Baruj, T. Kikuchi, S. Kajiwara, N. Shinya, Improved shape memory properties and internal structures in Fe-Mn-Si-based alloys containing Nb and C, J. Phys. IV France 11 (2003).

[10] A. Baruj, S. Kajiwara, T. Kikuchi, N. Shinya, Improvement of shape memory properties of NbC containing Fe–Mn–Si based shape memory alloys by simple thermomechanical treatments, Mater. Sci. Eng. A. 375 (2004).

[11] S. Kajiwara, D.Z. Liu, T. Kikuchi, N. Shinya, Remarkable improvement of shape memory effect in Fe-Mn-Si based shape memory alloys by producing NbC precipitates, Scripta Mater. 44 (2001).

[12] S. Kajiwara, D.Z. Liu, T. Kikuchi, N. Shinya, Development of Fe-Mn-Si based shape memory alloys with no necessity of "training", 11 J. Phys. IV France. (2001).

[13] H.C. Lin, K.M. Lin, S.K. Wu, T.P. Wang, Y.C. Hsiao, Effects of thermo-mechanical training on a Fe59Mn30Si6Cr5 shape memory alloy, Mater. Sci. Eng. A. 808 (2006) 438-440.

[14] F. Susan, H. Kenji, H. Kubo, Shape memory effect and crystallographic investigation in VN containing Fe-Mn-Si-Cr alloys, Mater. Trans. 45(3) (2005).

[15] N. Stanford, D.P. Dunne, Effect of second-phase particles on shape memory in Fe–Mn–Si-based alloys, Mater. Sci. Eng. A. 407 (2007) 454-455.

[16] Z. Wei, W. Yuhua, L. Ning, X. Wenling, W. Shanhua, Directional precipitation of carbides induced by γ/ε interfaces in an FeMnSiCrNiC alloy aged after deformation at different temperature, Mater. Sci. Eng. A. 459 (2007).

[17] N. Stanford, D.P. Dunne, H. Li, Re-examination of the effect of NbC precipitation on shape memory in Fe–Mn–Si-based alloys, Scripta Mater. 58 (2008) 583.

[18] C. Leinenbach, H. Kramer, C. Bernhard, D. Eifler, Thermo-mechanical properties of an Fe–Mn–Si–Cr–Ni–VC shape memory alloy with low transformation temperature, Adv. Eng. Mater. 14 (2012).

[19] O. Matsumara, T. Sumi, N. Tamura, K. Sakao, T. Furukawa, H. Otsuka, Pseudoelasticity in an Fe–28Mn–6Si–5Cr shape memory alloy, Mater. Sci. Eng. A. 279 (2000).

[20] M. Koyama, T. Sawaguchi, K. Ogawa, T. Kikuchi, M. Murakami, The effects of thermomechanical training treatment on the deformation characteristics of Fe–Mn–Si–Al alloys, Mater. Sci. Eng. A, 497 (2008).

[21] E.C. Oliver, T. Mori, M.R. Daymond, P.J. Withers, Neutron diffraction study of stress-induced martensitic transformation and variant change in Fe–Pd, Acta Mater. 51 (2003).

[22] R. Vaidyanathan, M.A.M. Bourke, D.C. Dunand, Texture, strain and phase fraction measurements during mechanical cycling in superelastic NiTi, Metall. Mater. Trans. A 32 (2001).

[23] P. Sittner, P. Lukas, D. Neov, M.R. Daymond, V. Novak, G.M. Swallowe, Stress-induced martensitic transformation in Cu-Al-Zn-Mn polycrystals investigated by two in-situ neutron diffraction techniques, Mater. Sci. Eng. A 324 (2002).

[24] B. Malard, P. Sittner, S. Berveiller, E. Patoor, Advances in martensitic transformations in Cu-based shape memory alloys achieved by in situ neutron and synchrotron X-ray diffraction methods, C. R. Phys 13 (2012) 280-292.

[25] E.C. Oliver, T. Mori, M.R. Daymond, P.J. Withers, Comparison using neutron diffraction of martensitic transformation in Fe–Mn–Si shape memory alloys with and without VN precipitates, Mater. Sci. Tech. 24 (2008) 902-907.

[26] M. Koster, W.J. Lee, C. Leinenbach, Cyclic deformation and structural fatigue behavior of an Fe-Mn-Si shape memory alloy, Materials Science & Engineering A 637 (2015) 29-39.

[27] W.J. Lee, R. Partovi-Nia, T. Suter, C. Leinenbach, Electrochemical characterization and corrosion behavior of an Fe-Mn-Si shape memory alloy in simulated concrete pore solutions, Materials and Corrosion 67(8) (2015) 839-846.

[28] W.J. Lee, B. Weber, G. Feltrin, C. Czaderski, M. Motavalli, C. Leinenbach, Phase transformation behavior under uniaxial deformation of an Fe–Mn–Si–Cr–Ni–VC shape memory alloy, Materials Science & Engineering A 581 (2013) 1-7.

[29] W.J. Lee, B. Weber, G. Feltrin, C. Czaderski, M. Motavalli., C. Leinenbach, Stress recovery behaviour of an Fe–Mn–Si–Cr–Ni–VC shape memory alloy used for prestressing, Smart Mater. Struct. 22 (2013).

[30] U. Stuhr, Time-of-flight diffraction with multiple pulse overlap. Part I: The concept, Nucl. Instr. Meth. Phys. Res. A 545(1-2) 319-329.

[31] N. Bergeon, G. Guenin, C. Esnouf, Microstructural analysis of the stress-induced ε martensite in a Fe–Mn–Si–Cr–Ni shape memory alloy: Part II: Transformation reversibility, 242 (1998) 87-95.

[32] A. Sato, E. Chishima, Y. Yamaji, T. Mori, Orientation and composition dependencies of shape memory effect in Fe-Mn-Si alloys, Acta Metall. 32(4) (1984) 539-547.

[33] A. Sato, K. Soma, T. Mori, Hardening due to pre-existing ε-Martensite in an Fe-30Mn-1Si alloy single crystal, Acta Metall. 30 (1982).

[34] V.V. Kokorin, L.E. Kozlova, A.N. Titenko, Temperature hysteresis of martensite transformation in aging Cu–Mn–Al alloy, Scripta Materialia 47 499-502.

[35] W.G. Burgers, J.A. Klostermann, Acta Met. 13 (1965).

[36] S. Sato, Y. Sunaga, T. Mori, Contribution of the γ -> ε transformation to the plastic deformation of stainless steel single crystals, Acta Metall. 25 (1977) 627-637.

[37] R.H.J. Hannink, M.J. Murray, Elastic moduli measurements of some cubic transition metal carbides and alloyed carbides, Journal of Materials Science 9(2) (1974) 223-228.

Figure captions:

Figure 1: SEM backscattered electron micrographs of a) SMA1 aged, b) detail view of SMA1 aged showing a grain boundary and precipitates, c) SMA7 and d) SMA7-2

Figure 2: Measurement setup of neutron diffraction during uniaxial loading. Planes which have their normal vector parallel to the loading direction fulfill the Bragg condition.

Figure 3: Stress strain characteristics for SMA1 aged, SMA7 and SMA7-2 recorded during interrupted in-situ neutron diffraction measurements

Figure 4: a) Full axial neutron diffraction spectra from samples in the undeformed state and after straining to 10 %, b) diffraction spectra in selected q-regime for step-wise increase of strain from 0 % until 10 %

Figure 5: Strain stress curve during interrupted quasistatic tensile test in a) and e), plots of normalized integrated intensity over stress in b) and f), plots of FWHM over stress in c) and g), plots of lattice strain as a function of stress in d) and h) for SMA1 aged and SMA7, respectively, capturing austenitic (111), (200), (220) and (311) grain families in axial alignment

Figure 6: a) Strain stress curve from interrupted cyclic test, b) and e) plot of normalized integrated intensity over stress, c) and f) plot of FWHM over stress and d) and g) plot of lattice strain over stress for the austenitic (220) and (200) grain orientations within SMA7-2.

Tables:

Table 1: Chemical composition and thermal treatments of monotonic and cyclic tensile tested samples

Table 2: Yield strengths of SMA1 aged, SMA7 and SMA7-2

Table 3: Grain orientation dependent Schmid factors for phase transformation and slip, elastic moduli for SMA1 aged and SMA7.